

Hot Oxidation Resistance of a Novel Cast Iron Modified by Nb and Al Addition for Exhaust Manifold Applications



GÜLŞAH AKTAŞ ÇELİK, Ş. HAKAN ATAPEK, ŞEYDA POLAT, MARIA-IOANNA T. TZINI, and GREGORY N. HAIDEMENOPOULOS

In this study, high-temperature oxidation behavior of ductile cast irons designed by Nb and Al addition (3.5 wt pct C, 4 wt pct Si, 1 wt pct Nb, 0 to 4 wt pct Al) is studied to develop an alloy that can perform better at elevated temperatures compared to commercial SiMo alloy. In the designed alloy, Mo is replaced by Nb as ferrite stabilizer and carbide former and has advantages compared to Mo since it does not form a network structure in the solidified matrix. Aluminum is added to the composition to inhibit the pearlite formation by causing inverse segregation of silicon that results in stabilizing ferrite and to obtain Al-rich protective oxide forms on the surfaces. Initially microstructural features of SiMo and designed alloys were examined, and modeling studies were carried out by Thermo-Calc software to determine the phases formed at high temperatures that are slightly below and above the A_1 temperatures of the alloys. Oxidation kinetics of SiMo and the designed alloys were determined by thermogravimetric analyses followed by oxidation tests at 750 °C, 800 °C and 850 °C in an air atmosphere furnace. The cross-sections and surfaces of the oxidized alloys were then characterized by microscopical studies and X-ray diffraction. The results revealed that all designed alloys exhibited better oxidation resistance at all studied temperatures than commercial SiMo alloy, and as aluminum addition increases, better performance is obtained because of the formation of Al-rich protective oxide layers. Thus, the designed alloys can be suggested as alternative exhaust manifold materials at elevated temperatures.

<https://doi.org/10.1007/s11661-022-06632-2>

© The Minerals, Metals & Materials Society and ASM International 2022

I. INTRODUCTION

IN the automotive industry, even though the requirements for lightweight materials have increased to save fuel and reduce emissions, iron-based cast components are still being used since they have relatively low cost and display reasonable mechanical properties.^[1–3] Although several non-ferrous alloys like aluminum^[4] and magnesium^[5] alloys and polymer-based composites^[6] can be good candidates for many automotive components due their low density and reasonable mechanical properties, in an exhaust system the major design criterion is high temperature resistance and mentioned materials cannot meet this requirement.^[7–9]

In an exhaust system, not only cast irons^[10,11] and stainless steels^[12,13] having ferritic and austenitic matrixes but also Ni-resist alloys^[14] can be used. Among these materials, SiMo ductile cast irons and their modified versions can be used to meet the stringent emission standards, environmental protection and fuel economy regulations.^[9,11] Their microstructure and mechanical properties undoubtedly play an important role in meeting these requirements. Commercial SiMo cast irons meet the ASTM A1095-15 specification and have graphite with varying morphology (spheroidal, compacted and mixed) embedded in a ferritic matrix. Such a microstructure provides high thermal conductivity, low coefficient of thermal expansion and good mechanical properties, which are used in the material selection index for an exhaust manifold.^[9,15,16] Exhaust manifolds are subjected to high temperatures and (i) high thermal conductivity material provides fast cooling, providing short-term exposure to operating temperature; (ii) low thermal expansion coefficient prevents cracks forming due to thermal fatigue^[3,17]; (iii) a stable microstructure guarantees good mechanical properties.^[18] Despite these advantages, SiMo cast irons can

GÜLŞAH AKTAŞ ÇELİK, Ş. HAKAN ATAPEK, and ŞEYDA POLAT are with the Department of Metallurgical and Materials Engineering, Faculty of Engineering, Kocaeli University, Umuttepe Campus, Kocaeli 41001, Turkey. Contact e-mail: gulsahaktas@gmail.com MARIA-IOANNA T. TZINI and GREGORY N. HAIDEMENOPOULOS is with the Laboratory of Materials, Department of Mechanical Engineering, University of Thessaly, Volos 38334, Greece.

Manuscript submitted October 14, 2021; accepted February 10, 2022.
Article published online April 3, 2022

only be used up to 820 °C due to their low A_1 temperature^[15] and low oxidation resistance.^[9] Thus, a new alloy design to overcome all aforementioned capabilities and shortcomings is needed.

Many studies can be found in the literature for modification of SiMo composition by changing silicon and molybdenum contents.^[9,19] Although high silicon content increases A_1 temperature and provides oxidation resistance by formation of Si-rich oxide layer at high temperatures, Gonzalez-Martinez *et al.* reported that the optimum silicon content in such alloys is limited by 5 wt pct since higher amounts make the alloy brittle.^[20,21] Molybdenum in the composition increases high-temperature tensile strength and resistance to thermal fatigue and creep due to the formation of a network of complex Fe-Mo carbides at grain boundary.^[3,22,23] However, like all the other carbide-forming elements, it is responsible for casting defects and embrittlement > 1 wt pct.^[3,10,23] In a novel cast iron composition alternative to commercial SiMo, other carbide-forming elements should be considered as well. A recent study by Aktaş Çelik *et al.* has concentrated on the effects of molybdenum, niobium, tungsten, vanadium, titanium and chromium in SiMo alloy, using thermodynamic simulations.^[24] Their results show that A_1 temperature increases by increasing the amount of these elements except for molybdenum. However, this increase does not exceed 7 °C and A_1 temperature can only reach to 842 °C by alloying 3 wt pct. In case of molybdenum, an increase is observed up to 1 wt pct, above which A_1 temperature starts to decrease. Previous experimental studies by Aktaş Çelik *et al.* showed that novel cast iron compositions having niobium or tungsten instead of molybdenum present higher A_1 temperatures compared to commercial SiMo cast iron.^[25,26] On the other hand, elements like chromium and aluminum are added to SiMo in some experimental studies, and the results provide knowledge about the optimum amounts that can be used without any detrimental effects on the properties.^[10,27,28] Chromium is a strong carbide-forming element and provides good oxidation resistance at compositions < 1 wt pct in SiMo cast irons.^[10] Above this composition, an undesirable fully carbidic microstructure is formed, as a result of which matrix is depleted in chromium causing poor oxidation resistance and brittleness.^[27] Another promising element is aluminum (up to 4 wt pct) that maximizes operating conditions by raising A_1 temperature^[25,26] and improves oxidation resistance by forming Al_2O_3 on the cast iron surface.^[9,27,29] Its effect on graphite content and morphology is well known; increasing aluminum in the composition, graphite formation can be inhibited, and its morphology has a variation in its nodularity.^[30,31] An increase in the amount of aluminum can have detrimental effects on mechanical properties, since it reveals a lattice distortion in bcc structure and shifts A_2 to B_2 (FeAl) and D_0_3 (Fe_3Al) crystal systems having higher yield and tensile strength but lower impact toughness.^[32]

In exhaust systems the utilized materials undergo decarburization and oxidation at high temperatures causing inverse effects on structural integrity. It is

known that surface oxidation of cast SiMo alloy can be inhibited by internal decarburization as a result of the reaction of carbon to form CO/CO₂ gas mixture, and not only outward diffusion of carbon but also inward diffusion of oxygen occurs simultaneously above 700 °C resulting in surface degradation.^[10,23,27] Under working conditions, controlling decarburization is possible only by metallurgical characteristics of the material, and an attempt to increase A_1 temperature by alloying is beneficial.^[11] Since carbon solubility in austenite is higher than in ferrite, an increased A_1 temperature will also help to decrease decarburization.^[11] Oxygen diffusion under the working conditions causes the pores left from graphite nodules to be filled with oxide scale; thus, the amount and morphology of graphite embedded in the cast matrix are important. On the other hand, iron and silicon in SiMo composition have a tendency toward outward diffusion to form the outer oxide layer (Fe_2O_3 , Fe_3O_4) and inner oxide layer (FeO, Fe_2SiO_4), which provides the protective effect. Additional alloying elements like aluminum and chromium have a similar behavior to form inner oxide layers (Al_2O_3 , Al_3FeO_4 , Cr_2O_3). Recent studies, focusing on varying the amounts of silicon, aluminum and chromium in the composition, show that decarburization can be suppressed, and thermally stable oxide films can be developed in air and in combustion atmosphere.^[3,10,11,23,27] Although good achievement is attained by several SiMo modifications,^[3,9,10,19,27] it is still not possible to use the cast alloy safely above 800 °C. This brings the requirement to develop novel cast iron compositions as suggested in our previous studies.^[24–26] Although thermodynamic modeling, solidification behavior and microstructural features of these new concept alloys are studied, their oxidation behavior has not been reported yet. In this study, oxidation of a novel cast iron having a composition of 3.5C-4Si-1Nb- x Al (x : 0 to 4 wt pct)^[25] is initially simulated by Thermo-Calc software, and then the cast compositions are exposed to air atmosphere at 700 °C to 850 °C. Experimental findings supported the simulated oxidation behavior of the alloys.

II. PROCEDURES

A. Materials

The SiMo alloy used in the study was received from a local company, produced as Y block by sand mold casting according to ASTM A 536-84 standard. The SiNb alloy and its aluminum-modified versions are also produced according to the same standard by using a similar casting route. In alloy casting, the charge is prepared with nodular pig iron (4.3 wt pct C, 0.7 wt pct Si), ferrosilicon (72 wt pct Si), ferroniobium (70 wt pct Nb) and DIN 1020 steel. Melting is carried out in a 35-kW Inductotherm induction furnace having a capacity of 25 kg. Pure aluminum is added according to the designed composition before the melting process is complete at 1560 °C. Both nucleation and spheroidization processes are simultaneously carried out in a SiC

crucible using nucleation agent (75 wt pct Si, 0.94 wt pct Ca, 1.68 wt pct Ce, 0.89 wt pct Al) and magnesium-rich alloy FeSiMg (45 wt pct Si, 7 wt pct Mg). The chemical composition is determined by optical emission spectrometer (OES, Foundary Master), and Table I shows the chemical compositions of all the cast alloys used in the study.

B. Methods

To determine the microstructural features of the cast alloys, standard metallographic procedures are performed, and the samples are etched by Nital (3 vol pct HNO₃). Microstructural characterization is carried out using both light microscope (LM, Olympus BX41M-LED), scanning electron microscope (SEM, Jeol JSM 6060) and energy-dispersive spectrometer (EDS, IXRF Systems Inc.).

The phases formed during oxidation are simulated by Thermo-Calc software using SSOL and SSUB databases for SiMo alloy (3.4 wt pct C, 3.6 wt pct Si, 0.8 wt pct Mo) and SiNb alloys (3.5 wt pct C, 4 wt pct Si, 1 wt pct Nb, 0 to 4 wt pct Al). In simulation studies, the oxidation test temperatures are selected as 750 °C and 850 °C, which are below and above the A₁ temperatures of the studied alloys. Weight fractions of the phases formed are monitored as a function of the partial pressure of oxygen at test temperatures.

To determine the oxidation behavior of the alloys, both thermogravimetric analysis (TGA, Netzsch STA 409 PG Luxx) and oxidation tests in furnace (MSA) are carried out at air atmosphere. For TGA, samples are machined to form cylindrical geometry having a 12 mm Ø and 3 mm, and their surfaces are mirror-like polished. In TGA, samples of 3.10 ± 0.30 g initial weight are then heated from room temperature to the test temperature (800 °C) at a rate of 10 °C s⁻¹, and weight changes are monitored for 24 h. The similar-sized mirror-polished samples are oxidized in a furnace at 750 °C, 800 °C and 850 °C for 24 hours and then cooled to room temperature in the furnace. Following the furnace tests, no spallation is observed on the surfaces. Both surfaces and cross-sections of the oxidized alloys are characterized by X-ray diffraction (XRD, Rigaku Ultima+) and SEM-EDS (Zeiss Evo10-IXRF) studies. XRD studies were carried out using Cu-K_α radiation, and a scanning speed of 1.0 °min⁻¹ is utilized.

III. RESULTS AND DISCUSSION

A. Microstructural Characterization

LM images of the cast alloys are given in Figure 1. Commercial SiMo matrix is Si-rich ferritic, having nodular graphite (G), pearlitic areas (P) and M₆C carbide (Figure 1(a)). Although SiMo matrix is designed to be ferritic and pearlite is not desired because of its detrimental effects, studies have shown that formation of pearlite cannot be avoided because of the inverse segregation of silicon.^[15,25,26] In the novel experimental alloys, although ferritic matrix is still present, the amount of pearlite is decreased by the addition of aluminum (Figures 1(b-d)). Earlier studies have shown that segregation behavior of silicon changes in such aluminum-added cast iron compositions, producing a preventing effect for the formation of pearlite.^[33–35] The microstructures of the cast alloys also reveal that by aluminum addition the amount and the morphology of graphite change. Aktaş Çelik *et al.* have reported that the amount of graphite embedded in the cast alloys (3.5 wt pct C, 4 wt pct Si, 1 wt pct Nb, 0 to 4 wt pct Al) decreases from 7 to 4 pct-area by increasing aluminum content up to 4 wt pct, which is comparable with the commercial SiMo alloy having 6.5 pct-area graphite.^[15,25] The change in graphite morphology of all the cast alloys, as compared to commercial SiMo alloy, can be followed by the change in nodularity, affecting the ductility, thermal conductivity/expansivity and damping capacity.^[36,37] According to DIN EN ISO 945-2 three types of graphite can be observed in ductile cast irons: (i) vermicular, (ii) irregular spheroidal and (iii) spheroidal (nodular). In the studied SiMo alloy, 5 pct vermicular, 35 pct irregular spheroidal and 50 pct spheroidal graphite morphologies are observed, excluding the unidentified components within the matrix.^[31] Aktaş Çelik *et al.* have examined all types of graphite morphologies on aluminum-modified cast irons, and the dominant one is observed to be irregular spheroidal (54 to 48 pct). By the addition of aluminum, both irregular spheroidal and spheroidal graphite (30 to 20 pct) have decreased, and vermicular graphite (11 to 20 pct) has increased. The change of spheroidal morphology of graphite to vermicular is affected by Mg/S ratio; however, blocking effect of aluminum to carbon diffusion by surrounding the graphite phase is a more distinctive cause in these alloys.^[25]

Table I. Chemical Compositions of the Cast Alloys (Wt Pct)

Alloy	C	Si	Mo	Nb	Al	Mg	Mn	P	S
SiMo	3.40	3.60	0.80	—	—	0.042	0.150	0.030	0.015
SiNb	3.57	4.04	—	0.96	0.02	0.074	0.231	0.057	0.028
SiNb-1Al	3.46	3.96	—	0.97	0.97	0.082	0.235	0.059	0.028
SiNb-2Al	3.47	3.99	—	1.03	2.03	0.078	0.245	0.057	0.032
SiNb-3Al	3.52	4.07	—	1.02	3.05	0.081	0.225	0.058	0.028
SiNb-4Al	3.54	4.05	—	1.04	4.03	0.079	0.228	0.055	0.035

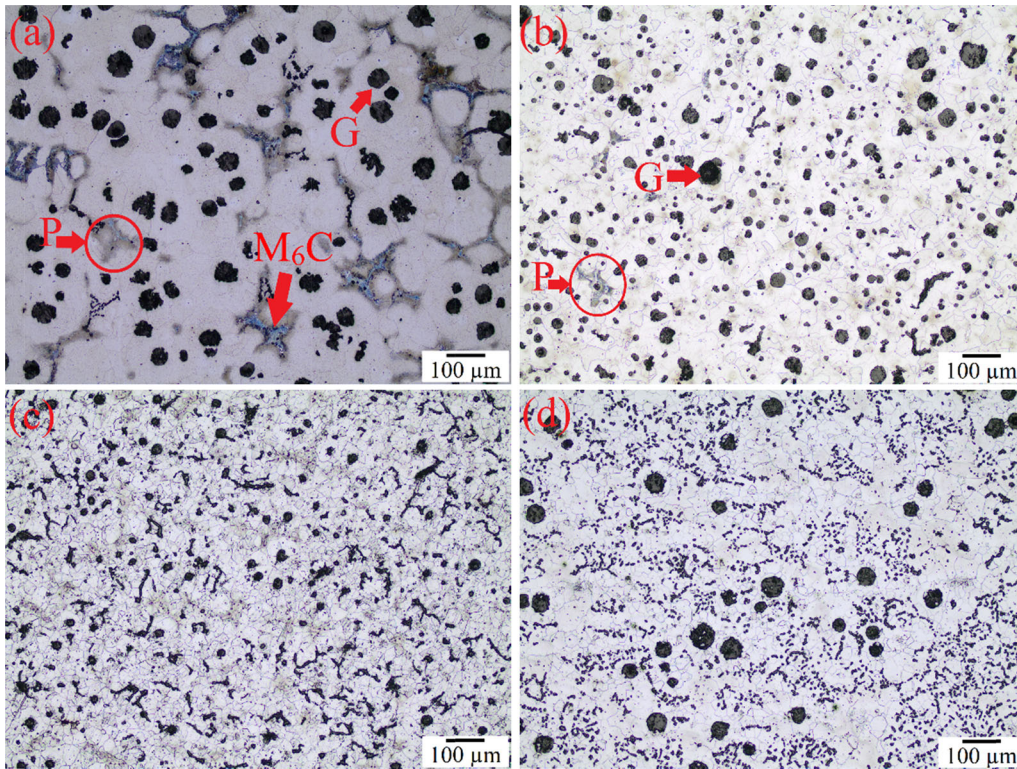


Fig. 1—LM images showing the microstructures of the alloys: (a) SiMo, (b) SiNb, (c) SiNb-2Al, (d) SiNb-4Al.

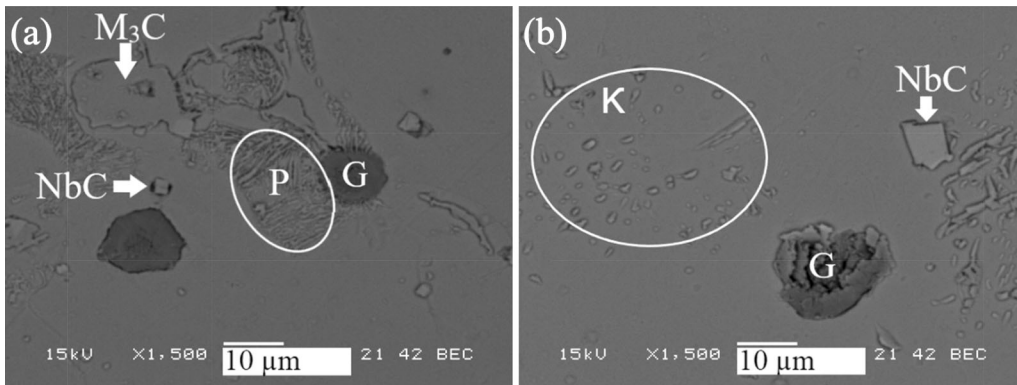


Fig. 2—SEM images showing the microstructures of the alloys: (a) SiNb and (b) SiNb-4Al.

The solidified structure of SiNb alloy is shown in the SEM image given in Figure 2(a), where some microstructural features like pearlite and carbides embedded in ferritic matrix are seen. Aktaş Çelik *et al.* have reported that during solidification of this cast alloy, a primary carbide (NbC) precipitates at 1321 °C directly from the liquid and has faceted morphology.^[25] During solidification, liquid-austenite interface (cell boundaries) can be enriched by the positive segregation of carbide forming elements (Fe, Nb) and a ledeburitic structure consisting of austenite and carbides is formed as a result of eutectic reaction.^[38,39] As indicated in Figure 2(a), the cast alloy has both NbC primary carbide (6.44 wt pct C, 90.84 wt pct Nb, 2.28 wt pct Fe, 0.10 wt pct Si, 0.11 wt pct Mn)

with faceted morphology and Fe-rich M_3C type carbide (19.17 wt pct C, 77.70 wt pct Fe, 0.99 wt pct Si, 0.94 wt pct Mn, 1.20 wt pct Cr). M_3C type carbide is formed as a component of eutectic (ledeburite) structure. In the final microstructure, austenite in the ledeburitic structure transforms to pearlite by eutectoid reaction.^[39,40] The formation of carbides can be attributed to both chemical composition and segregation of the elements. Likewise, a similar phenomenon is expected, and aluminum-rich precipitates (kappa phase, κ) form during crystallization in aluminum (above 4 wt pct) modified alloys.^[32] The formation of kappa (κ) phase is observed within the matrix of cast alloy having the highest aluminum content (Figure 2(b)).

B. Oxidation Modeling

Thermodynamic simulations help to determine decarburization and the stable oxide phases that can form at given temperatures and partial oxygen pressures. It is known that $\log pO_2$ is between -25 and 0 in the service conditions of the exhaust manifolds.^[10,23] However, simulations given in Figure 3 are carried out starting from lower partial pressure values (-40) to follow the decarburization and oxidation processes. Below the A_1 temperature (750 °C) of the commercial SiMo alloy, decreasing iron content can be followed, and decarburization is revealed by oxidation of graphite phase, as $\log(pO_2)$ changes from -40 to -25 (Figure 3(a)). Although FeSi and Mo_2C phases are not observed within the cast structure, they are stable in this pressure range. Due to oxidation and decarburization, these phases transform to oxide phases as the partial pressure of oxygen increases. The presence of β - SiO_2 in this range can be attributed to oxidation of FeSi. Above A_1 temperature (850 °C), although similar metallurgical phenomena like decarburization and oxidation take place, graphite phase dissolves and Fe_3C becomes stable as shown in Figure 3(b). In the range of service conditions, FeO, Fe_2SiO_4 , Fe_3O_4 and Fe_2O_3 phases form in the SiMo oxide scale at both temperatures (Figure 3). The oxide scale consists of multi-layers in ductile cast irons; the inner layer forms by the diffusion of oxygen from surface to the substrate while the outer layer forms by the diffusion of iron from substrate to the surface.^[10,11,27] The oxygen partial pressure, where the oxide phase is stable, determines the sequence of formation of oxide phases. In the outer layer, Fe_2O_3 and Fe_3O_4 phases form first because of their higher oxygen partial pressures. FeO and Fe_2SiO_4 form in the inner layer as oxygen partial pressure decreases. The presence of the silicon causes the formation of unstable SiO_2 at the inner layer. Its reaction with Fe, O and FeO forms the Fe_2SiO_4 phase, which is denser than iron oxide phases providing better oxidation resistance.^[11] The oxides like MoO_2 , $FeMoO_4$ and MoO_3 , having no barrier effect, can be formed as well because of internal

oxidation (Figure 3). Although the amount and type of oxide phases are the same at 750 and 850 °C, it is clear that their formation shifts to higher pO_2 as expected, indicating that stable oxide phases form more easily at higher temperature.

The simulated data of modified cast alloys (SiNb- x Al) indicating the variation of weight fractions of phases as a function of $\log(pO_2)$ at 750 °C are given in Figure 4. To emphasize the effect of aluminum addition, the figures are given separately for 0, 1, 3 (Figure 4(a)) and 0, 2, 4 wt pct Al additions (Figure 4(b)). Similar to SiMo alloy, decreasing iron content, decarburization and formation of β - SiO_2 are observed as $\log(pO_2)$ changes from -40 to -25 . Within the range of working conditions, the effect of increasing aluminum addition directly appears by the decrease of the amount of iron oxides (Figure 4). Besides, the amount of Fe_2SiO_4 , providing oxidation resistance in such compositions, also decreases in the inner oxide layer since aluminum-rich oxides (Al_2SiO_5) can be formed. At higher $\log(pO_2)$ values, namely at the outer oxide layer, decrease of Fe_2O_3 and Fe_3O_4 can be attributed to the formation of Al_2FeO_4 phase. Phases such as Al_2SiO_5 ^[41] and β - SiO_2 ^[42,43] can also be present in the outer layer (Figure 4).

The simulations concerning the weight fraction of phases as a function of $\log(pO_2)$ are also studied at 850 °C (Figure 5), and the amount of iron decreases because of the formation of FeSi and Fe_3C at low $\log(pO_2)$. In this pressure range (-40 to -25), the presence of graphite and formation of β - SiO_2 are also seen. As the pressure increases, the presence of FeO is observed, which drops drastically by the formation of Fe_2SiO_4 and Al_2SiO_5 . In the inner oxide layer, as the amount of aluminum increases, FeO amount keeps decreasing, Al_2SiO_5 increases and Fe_2SiO_4 does not change. Although the presence of silicon in the composition provides oxidation resistance by forming a stable Fe_2SiO_4 layer, it is not sufficient at higher operation temperatures. Thus, alloying elements such as aluminum and chromium forming stable oxide layers

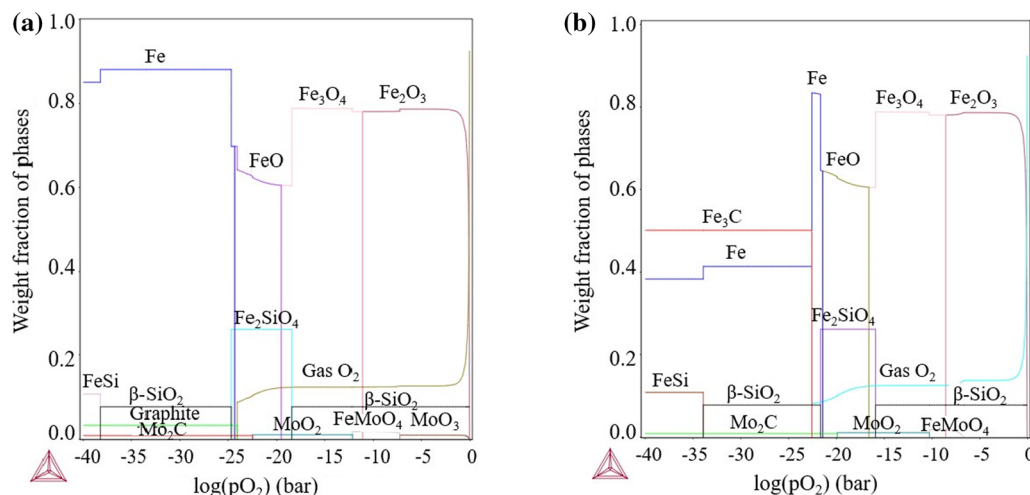


Fig. 3—Phases formed during oxidation of SiMo alloy with respect to oxygen partial pressure: (a) 750 °C and (b) 850 °C.

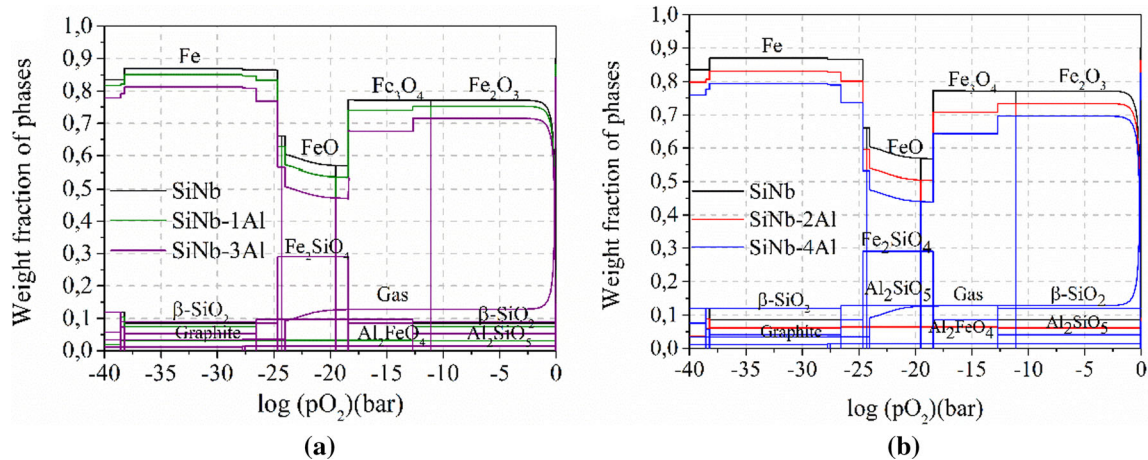


Fig. 4—Phases formed during oxidation of SiNb- x Al alloys with respect to oxygen partial pressure at 750 °C; (a) x : 0, 1, 3 and (b) x : 0, 2, 4 (wt pct).

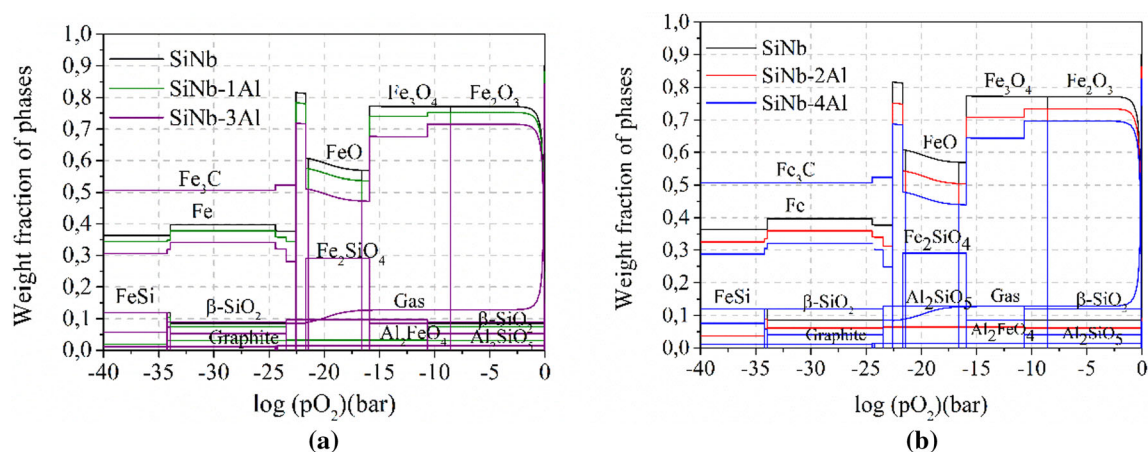


Fig. 5—Phases formed during oxidation of SiNb- x Al alloys with respect to oxygen partial pressure at 850 °C; (a) x : 0, 1, 3 and (b) x : 0, 2, 4 (wt pct).

are needed.^[10,27] When the higher $\log(pO_2)$ (above -15) is considered, the protective characteristics of aluminum addition can be also observed easily by the decrease of iron oxides and increase in the aluminum-rich oxides in the outer oxide layer.

A schematic presentation of the oxide scales formed on the alloy surfaces at 750 °C and 850 °C is given in Figure 6 for the studied alloys as a function of oxygen pressure. Calculations show that the components in the oxide scale do not change for all alloy compositions at both temperatures. This schema indicates the types of oxides formed on the substrate from surface to the gas (O_2) atmosphere. The oxide scale on SiMo contains β -SiO₂, FeO, Fe₂SiO₄, Fe₃O₄ and Fe₂O₃, which are commonly seen oxide phases.^[42,43] The oxide scale on SiNb consists of the same oxides as in SiMo. Aluminum-rich oxides (Al₂SiO₅, Al₂FeO₄) are present together with the iron oxides (FeO, Fe₃O₄, Fe₂O₃) and silicon-rich oxides (β -SiO₂, Fe₂SiO₄) for SiNb-4Al alloy.

C. TGA on Oxidation

TGA is used to determine the oxidation behavior of SiMo and SiNb alloys at 750 and 850 °C, which have been used in modeling studies, and the obtained data are given in Figure 7. Below the A₁ temperature (750 °C), during the initial 100 min, weight change due to rapid oxidation and decarburization is observed for SiMo alloy. A linear oxidation behavior is displayed after 100 min up to about 700 min, and in progressing time the formation of a stable oxide layer causes a decrease in the rate of oxidation. A similar trend in weight change during the initial 100 min is seen at higher test temperature (850 °C) for SiMo alloy. However, in the linear region a higher oxidation rate appears within the period between 100 and 250 min compared to the lower test temperature (750 °C). Beyond 250 min, a continuous decrease in weight can be explained by the decarburization of graphite phase and austenitic matrix at the studied temperature.^[36,37]

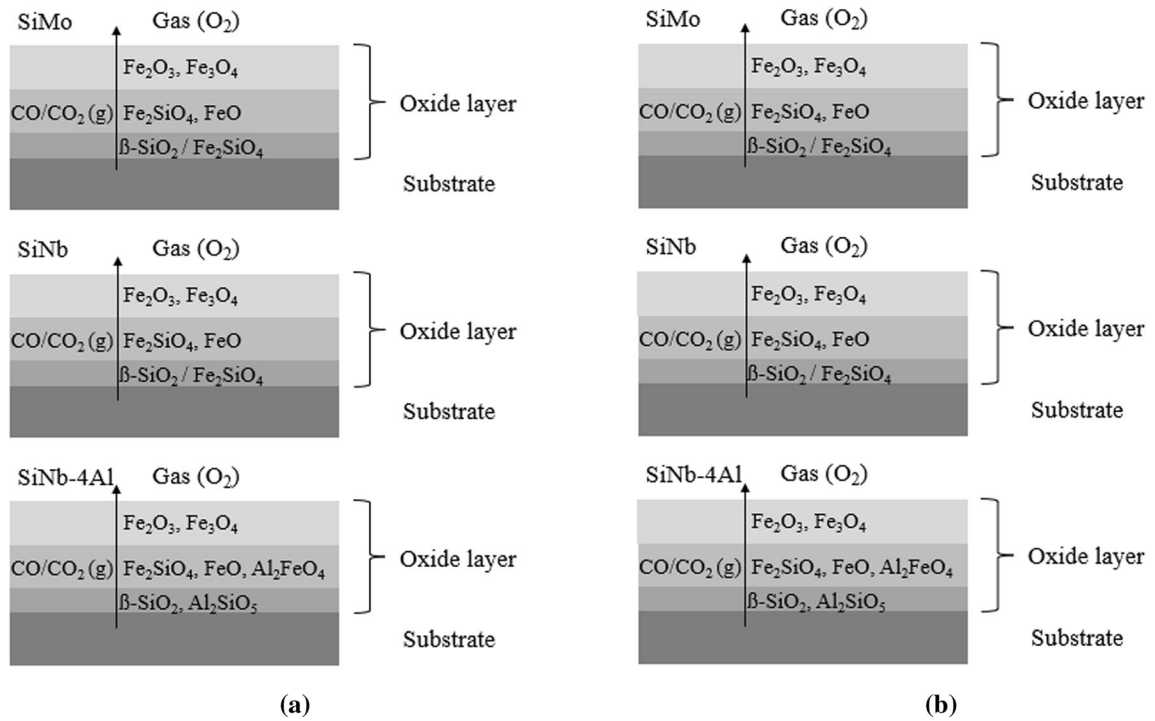


Fig. 6—Schematic presentation of the oxide scales formed on the alloy surfaces; (a) 750 °C and (b) 850 °C.

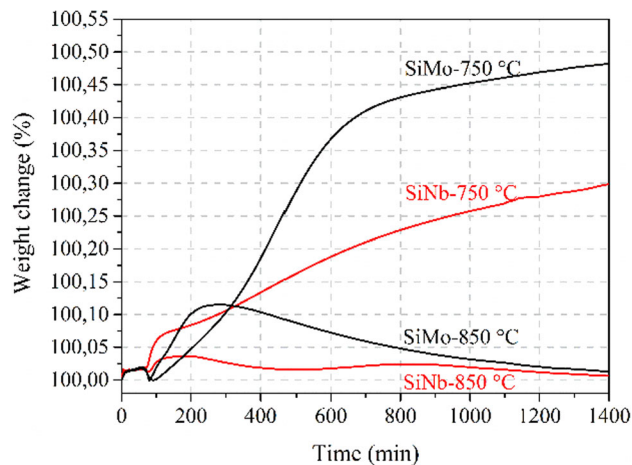


Fig. 7—TGA curves of oxidation tests of SiMo and SiNb alloys at 750 °C and 850 °C.

Although the weight gain of SiNb alloy is comparatively lower than that of SiMo alloy, a similar trend is observed (Figure 7). In the initial 100 min, weight gain is seen at 750 and 850 °C because the oxidation of metal and decarburization is very small. At 750 °C after 100 min, a linear jump in weight gain is observed, which is followed by a parabolic curve at a lower rate. SiO₂ layer forms between 600-800 °C, and this layer is damaged by the growing FeO nodules; the reaction between FeO and SiO₂ causes the rapid enlargement of the Fe₂SiO₄ layer.^[43,44] On the other hand, at this temperature, lack of a stable SiO₂ layer may result in continuous metal oxidation. As the temperature increases, SiO₂ phases form at the metal-oxide interface, and these dense and

homogeneous phases act as a barrier layer inhibiting oxidation.^[11,43] Recently, Ebel *et al.* emphasized the protective characteristics of SiO₂ layer that is obtained above 800 °C.^[44] A similar jump after 100 min is seen at 850 °C for SiNb alloy, beyond which weight loss due to the decarburization of both graphite and austenitic matrix is the dominant mechanism. As is well known, the oxidation kinetics change depending on the stability and permeability of the oxide layer formed on the metal surface.^[43,44] In cast irons, the iron oxides formed on the surface at elevated temperatures are porous structures which cannot provide a barrier effect for good stability and permeability. However, the presence of finer and denser Si-rich oxide layers on the surface decreases oxygen penetration and provides higher oxidation resistance.^[42-44] This effect can be clearly seen by the slopes of the oxidation curves given in Figure 7, and SiNb alloy containing higher silicon has a lower oxidation rate due to the formed Si-rich oxide layers (Fe₂SiO₄ and SiO₂). As a result, the weight increase at the end of the tests is lower for SiNb alloy at 750 °C, and the highest weight gain at 850 °C is also lower for SiNb alloy.

Considering the service conditions of diesel engines where cast steels are preferred,^[2,3] the oxidation behavior of aluminum-modified SiNb alloys is studied at 800 °C, which is just below the A₁ temperature of SiNb. Thus, the decarburization of austenite phase in the modified alloys is eliminated. The variation of weight with respect to oxidation time is given in Figure 8. Same phenomena are observed in the first 100 min for the aluminum-modified alloys, like initial oxidation of the metal followed by decarburization of the graphite phase. At 800 °C, the metal oxidation rate of SiNb alloy shows

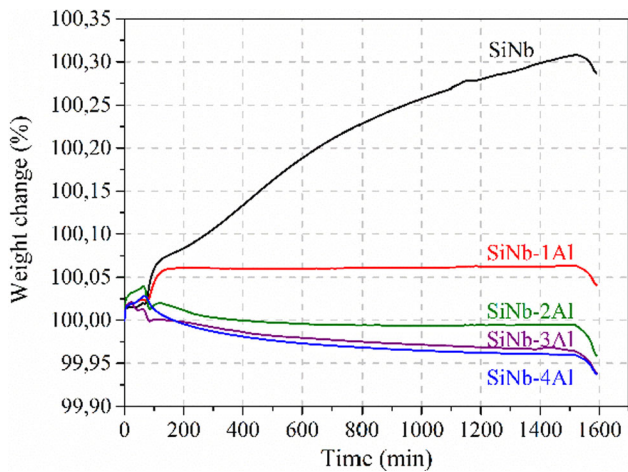


Fig. 8—TGA curve of aluminum-modified SiNb-xAl cast alloys at 800 °C.

a sharp increase and then continues with a slower rate due to formation of Si-rich oxides, at prolonged oxidation times. However, as aluminum is added to the composition, a sharp decrease in weight change is observed because of the barrier effect of aluminum-rich oxides. Besides the formation of aluminum-rich oxide layers, the decrease in weight due to oxidation can also be attributed to the oxidation and decarburization of graphite that are in contact with oxygen at the surface. Oxidation of graphite causes the formation of voids providing the transport of oxygen to the metal matrix, and these voids also act as new surfaces having high reaction capability with oxygen. In this case, barrier oxide layers can be formed at these new surfaces preventing further oxidation. Thus, the decrease in weight change is only due to the oxidation of graphite. Several studies confirm this argument for the barrier effect of Al, Cr and Si-rich oxides on inhibiting the oxidation of metal around graphite voids in ductile cast irons tested at elevated temperatures.^[10,27,42–44] Not only the distribution of graphite but also its morphology plays an important role in oxidation kinetics. Studies revealed that vermicular graphite morphology causes higher oxygen transfer to the metal matrix resulting in higher oxidation compared to the nodular ones.^[43]

D. Characterization of Oxidized SiMo and SiNb Surfaces

The cross-sections of the SiMo and SiNb alloys oxidized at 750 °C and 850 °C for 24 hours at air atmosphere are given in Figure 9. When the oxide morphologies of SiMo alloy are examined, it can be clearly seen that outer and inner layers with different contrasts exist (Figure 9(a)). The inner layer visible in dark contrast is formed by the diffusion of oxygen from the surface and consists of graphite and carbide phases. Studies have shown that inner layer consists of FeO and Si-rich Fe₂SiO₄/SiO₂ oxides.^[42,44] The outer layer visible in light contrast is formed by the diffusion of iron toward the surface and consists of Fe₃O₄ and Fe₂O₃

oxides.^[10,43] In these ductile cast irons, oxidation proceeds toward the matrix by the oxidation of graphite nodules as seen in Figure 9(b). Fe-rich oxide nodules form by two different mechanisms. In the first mechanism, nodules grow simply by the expansion of the iron oxides at the initial stage of the oxidation. In the second mechanism, the thin protective layer fractures locally and oxidizing gases penetrate through the subsurface defects and cause the nucleation and growth of the nodules under the failed protective layer.^[42] These nodules can grow rapidly around the graphite,^[42] and they are visible in distinctive contrasts as seen in Figure 9(b). Similar oxide layers are observed on the surface of SiNb alloy as well, at all the studied test temperatures (Figures 9(c) and d). Voids are also seen in both inner and outer layers. While the outward diffusion of iron causes voids in the inner layer,^[10] the voids in the outer layer are caused by the oxidation of graphite.^[43]

SEM analysis is carried out to study the oxidized surfaces at 750 °C and 850 °C in detail. The detachment between the outer and inner layers can be clearly seen in the Figure 10(a), since they have different thermal expansion coefficients and weak adherence. In Figure 10(b), a thicker oxide layer having voids and graphite nodules is observed because of the increase in test temperature. The progression of oxidation into the matrix through graphite nodules can be examined in Figure 11(a). Despite the thin and stable protective layer on the surface of SiNb alloy tested at 750 °C, graphite nodules located close to the surface act as oxidation sites. Due to the higher silicon content of SiNb alloy, Si-rich oxides form at the interface between graphite and metal matrix inhibiting the further progress of oxidation.^[37,43] This inhibiting effect is proven by the presence of non-oxidized graphites near the surface (Figure 11(a)). During oxidation, a part of graphite is volatilized by oxidation,^[45] and it is referred as oxidized graphite, as a result of which carbon content of graphite decreases down to 1.95 wt pct. As the temperature increases, the thickness of oxide layer increases, and more porous structure appears because of increased number and size of the voids (Figure 11(b)). In Figure 12, the thickness variations of the oxide layers on SiMo and SiNb alloys are given as a function of test temperature. Although in both alloys oxide layer thicknesses increase by the increasing temperature, SiNb alloy has a tendency to form a thinner oxide layer compared to SiMo alloy. This tendency can be attributed to the presence of higher amounts of silicon in SiNb alloy, since Si-rich oxides in the inner layer prevent the formation of iron-rich oxides.^[10,42–44,46]

The XRD patterns (not shown) highlighting the presence of oxide phases (FeO, Fe₂O₃, Fe₃O₄ and Fe₂SiO₄) formed on the surfaces of the alloys tested at all temperatures are similar to those obtained by the thermodynamic calculations (Figures 4 and 5). SEM studies on the cross-sections of the alloys revealed the presence of layered oxide structure, and recent works have shown that the outer layer consists of Fe₂O₃ and Fe₃O₄ while the inner layer includes FeO and Fe₂SiO₄ phases.^[43,44]

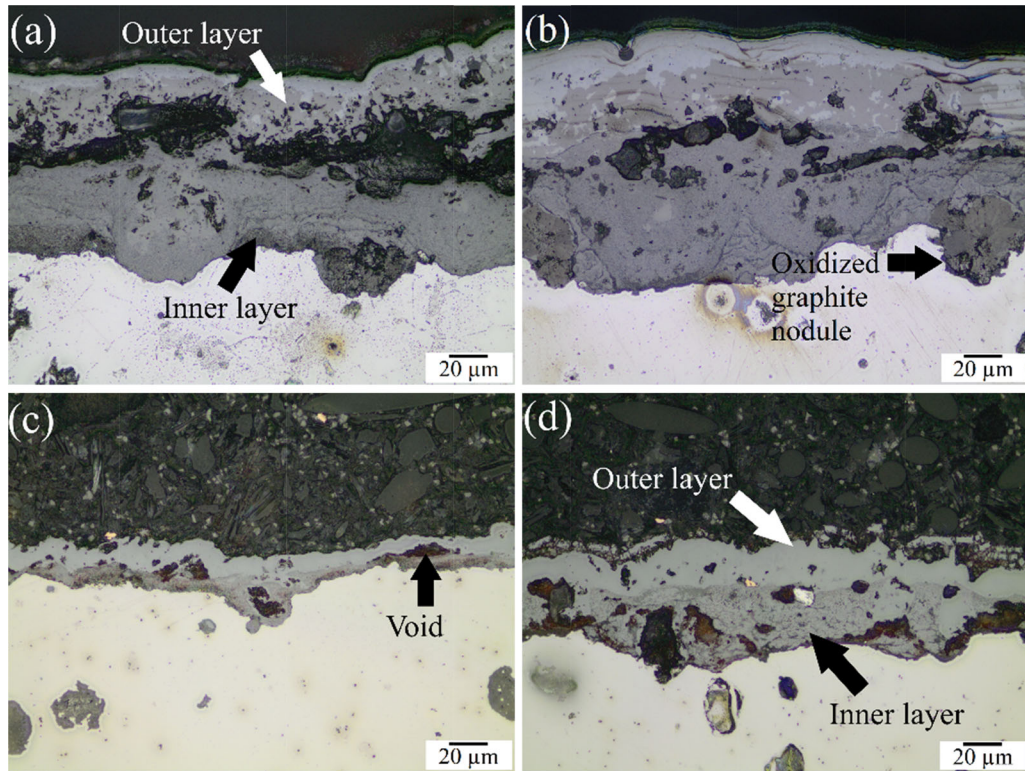


Fig. 9—LM images showing the cross-sections of oxidized SiMo (*a* and *b*) and SiNb (*c* and *d*) alloys. Test temperature: (*a* and *c*) 750 °C and (*b* and *d*) 850 °C.

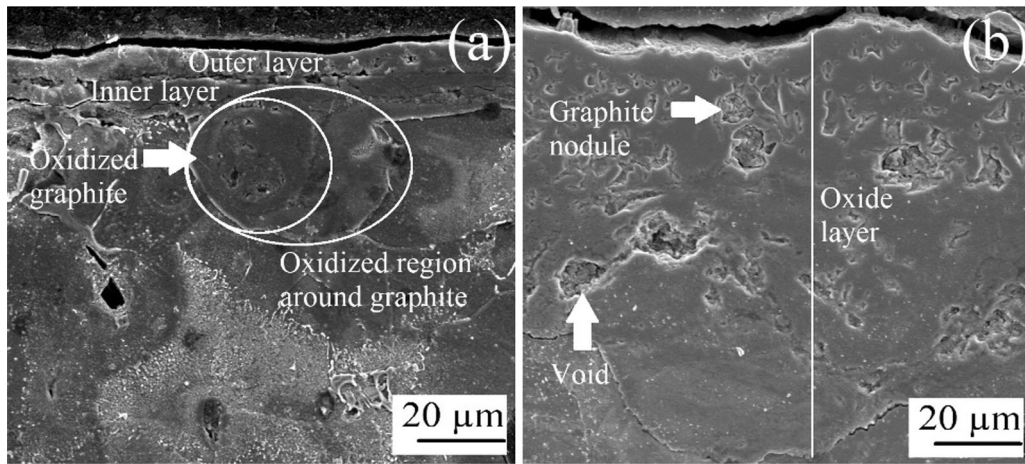


Fig. 10—SEM images showing the cross-sections of oxidized SiMo alloy; (*a*) 750 °C and (*b*) 850 °C.

E. Characterization of Oxidized SiNb-*x*Al Surfaces

The LM images showing the cross-sections of aluminum-modified SiNb alloys oxidized at 750 °C, 800 °C and 850 °C at air atmosphere are given in Figures 13, 14 and 15, respectively. The protective layer is formed by oxide nodules at lower aluminum additions whereas it gains a continuous characteristic at higher aluminum contents (Figures 13(a) and b). By the addition of aluminum, protective aluminum-rich oxides ($\text{AlFeO}_4/\text{Al}_2\text{O}_3$) form besides FeO and Si-rich $\text{Fe}_2\text{SiO}_4/\text{SiO}_2$ oxides in the inner layer.^[29,47] The type

and thickness of the Al-rich oxides depend on the amount of aluminum in the composition. Tomaszewicz and Wallwork^[48] have shown that although the outer oxide layer consists of iron-rich oxides and Al_2O_3 in Fe-Al alloys, the most efficient protective Al_2O_3 layer occurs at higher aluminum content than 6.9 wt pct. As aluminum increases, the formation of Fe-rich oxides is inhibited because of the barrier effect of Al-rich oxides. This is due to the slowed diffusion of iron and oxygen causing a thinner Fe-rich oxide layer.^[9,10,41–43]

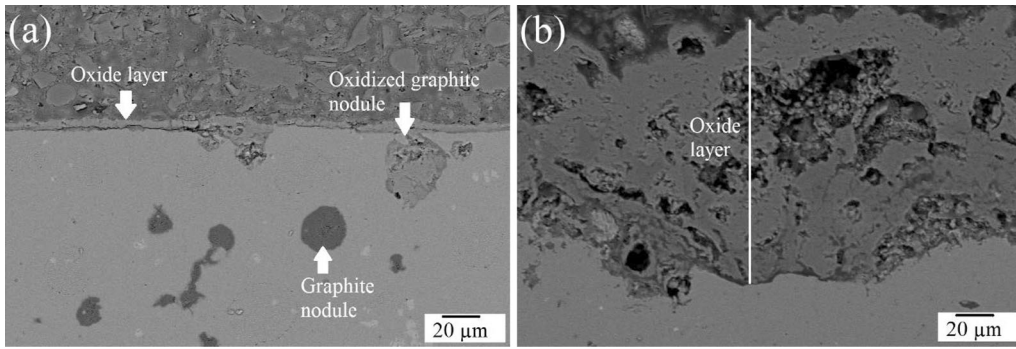


Fig. 11—SEM images showing the cross-sections of oxidized SiNb alloy; (a) 750 °C and (b) 850 °C.

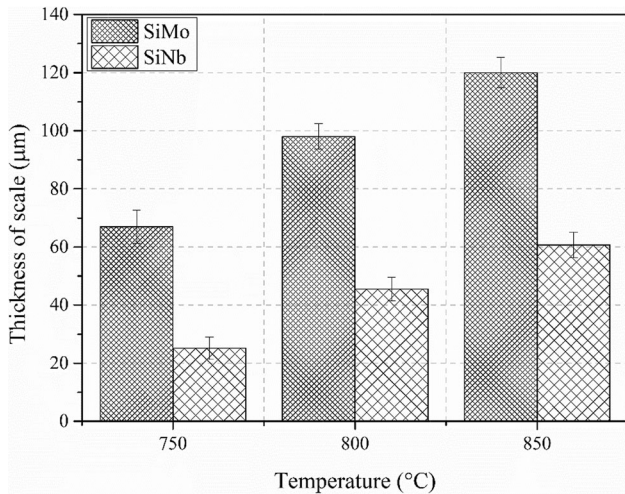


Fig. 12—Thickness variation of the oxide layers on SiMo and SiNb as a function of test temperature.

The increase in oxidation rate at higher temperature (800 °C) causes the formation of a thicker oxide layer (Figure 14). At lower aluminum content, oxide nodules form around the graphite nodules within the oxide layer (Figure 14(a)), and the layer becomes continuous as aluminum increases in the composition (Figure 14(b)). Similar to the 750 °C results, the oxidation progresses through vermicular graphite. At the highest test temperature, 850 °C, the thickness of the oxide layer is higher, and double-layered scale is clearer (Figure 15). Oxidation progresses through the graphite in this case as well, besides the voids formed because of decarburization of graphite. Specifically, a recent study on the oxidation behavior of aluminum-modified SiMo ductile cast iron revealed that the amount of oxygen used for decarburization increased as the temperature reached 800 °C and voids were formed by decarburization of nodular and vermicular graphite particles.^[27]

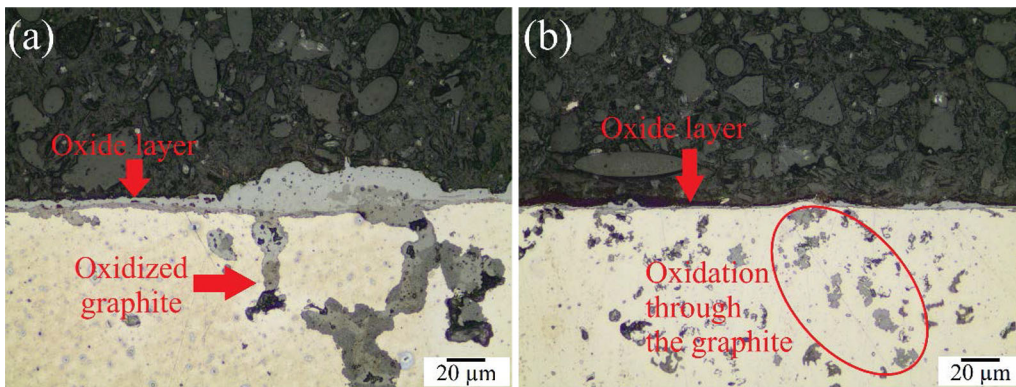


Fig. 13—LM images showing the cross-sections of the alloys oxidized at 750 °C for 24 h; (a) SiNb-1Al and (b) SiNb-4Al.

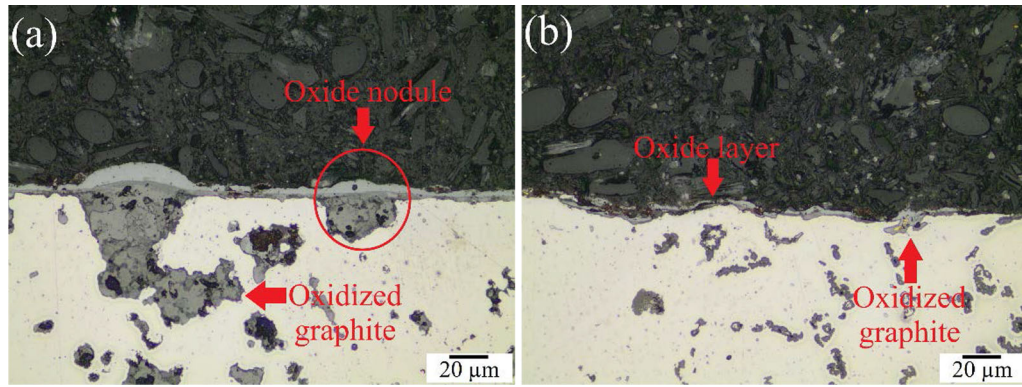


Fig. 14—LM images showing the cross-sections of the alloys oxidized at 800 °C for 24 h; (a) SiNb-1Al and (b) SiNb-4Al.

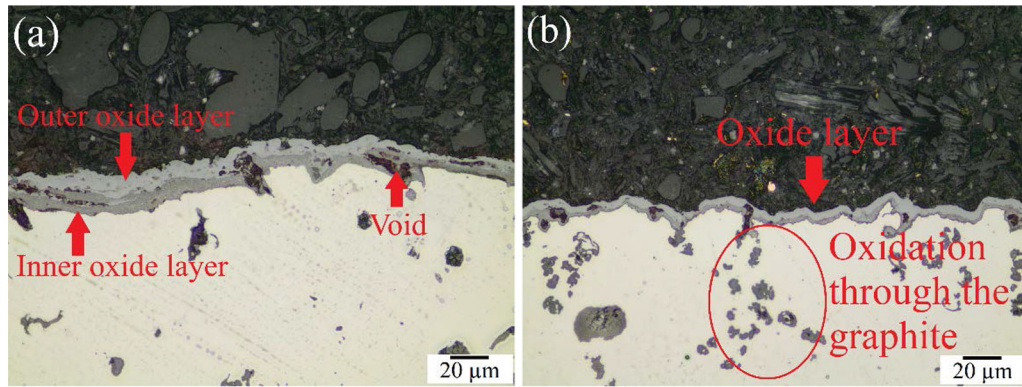


Fig. 15—LM images showing the cross-sections of the alloys oxidized at 850 °C for 24 h; (a) SiNb-1Al and (b) SiNb-4Al.

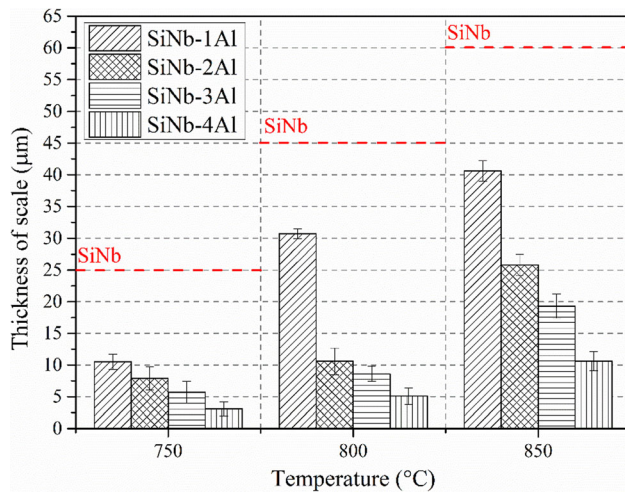


Fig. 16—Thickness variation of the oxide layers on SiNb-*x*Al alloys as a function of test temperature.

Thickness variation of the oxide scale by addition of aluminum is given in Figure 16 where the level of SiNb alloy is shown by the dotted line. The barrier effect of Al-rich oxides appears by the decrease in scale thickness as aluminum content increases. The oxidation behavior is also determined by the graphite morphology; it has

been shown that vermicular type graphite causes the progress of oxidation toward the matrix and causes formation of voids due to decarburization.^[27] The amount of vermicular graphite increases by increasing aluminum content in SiNb alloys.^[25] This effect can be seen at all the test temperatures as shown in Figures 13-15, where the oxidation progresses toward the matrix through the vermicular graphite, especially at higher aluminum additions. Temperature is the critical parameter for determining the types of oxides to be formed and their amounts. The increasing temperature causes the faster diffusion of oxidizing agents, thereby increasing the oxidation rate.^[44]

To observe the effects of test temperature and aluminum content on the oxidation behavior of the modified SiNb alloys, oxidized cross-sections of the alloy having highest aluminum addition (SiNb-4Al) are studied using SEM (Figure 17). In the BSE-SEM image of the alloy oxidized at 750 °C, a thin and homogeneous oxide layer adhered at the surface is observed, and oxidation progresses through the vermicular graphite toward the metal matrix (Figure 17(a)). The characteristics of the oxide layer formed at 800 °C change as shown in Figure 17(b); a thin, porous oxide layer covers the whole surface. Despite the barrier effect of aluminum-rich oxide, oxidation progresses toward the matrix through the graphite phase. The increase in

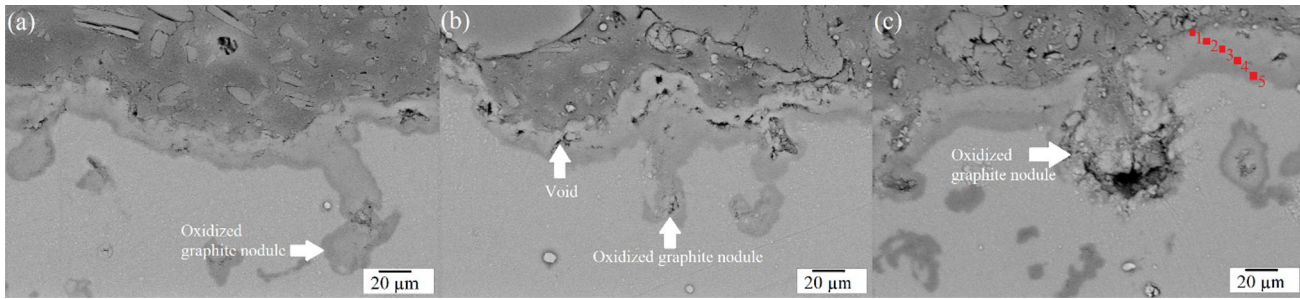


Fig. 17—SEM images showing the oxidized SiNb-4Al alloy at (a) 750 °C, (b) 800 °C and (c) 850 °C.

Table II. EDS Data (Wt Pct) for the Labeled Points in the Cross-Section of Oxidized SiNb-4Al Alloy at 850 °C

Point	Fe	C	Al	Si	O
1	70.42	14.96	2.59	2.13	9.90
2	71.64	12.07	2.62	5.08	8.58
3	81.20	8.12	2.95	2.94	4.79
4	72.60	10.70	5.80	2.66	8.24
5	61.98	12.95	12.8	3.68	8.59

temperature causes the formation of voids in the oxide layer resulting in a porous structure (Figure 17(b)). The results for the highest test temperature (850 °C) are given in Figure 17(c). Due to the increased diffusion rate of the oxidizing agents, the oxide layer is comparatively thicker and contains voids. Also, oxidation progresses deeper toward the matrix through the graphite phase, and formation of the void around the oxidized graphite nodule can be clearly seen in Figure 17(c). The EDS studies are carried out to determine the presence of the aluminum in the oxide layer, which provides a barrier effect during the oxidation test. The results are given in Table II for the points labeled in Figure 17(c). The obtained data indicate that the oxide layer is rich in iron and has both aluminum and silicon, where aluminum content increases from surface to metal matrix. These findings are in agreement with the current literature that reports the presence of aluminum-rich oxides at the oxide layer-metal interface,^[9,41] and as the aluminum content increases at the interface Al₂O₃ oxide can be formed as a protective layer.^[27]

The XRD patterns (not shown) highlighted that, like the oxidized SiMo and SiNb alloys, iron and iron-silicon oxides such as FeO, Fe₂O₃, Fe₃O₄ and Fe₂SiO₄ are present on the surfaces of SiNb-*x*Al alloys. However, the presence of aluminum causes the decrease in the intensity of ferrous oxides. At all test temperatures, Al₂SiO₅, Al₂FeO₄ and AlFeO₃ phases are detected, and these phases are responsible for the decrease of outward diffusion of iron and inward diffusion of oxygen, causing a decrease in the thickness of the Fe-rich oxide layer. The presence of α -Fe phase in the XRD diffractogram is attributed to the thinner Fe-rich oxide layer on the surface.

IV. CONCLUSION

In this study, alternative exhaust manifold materials were designed using Nb and Al elements in ductile cast iron compositions, and their high-temperature oxidation behaviors were studied. The findings can be summarized as follows:

1. By replacing Mo with Nb, the formation of eutectic carbides was inhibited, and SiNb alloy having higher Si content exhibited MC carbides dispersed in fully ferritic matrix. Al addition to the SiNb alloy resulted in the deterioration of nodular morphology of graphite. At the highest Al concentration (*x*: 4 wt pct), the precipitation of kappa phase was observed.
2. In the simulations, SiMo and SiNb alloys had similar oxide phases (Fe₂O₃, Fe₃O₄, FeO, Fe₂SiO₄) at 750 and 850 °C. However, as aluminum was added to the SiNb alloy, weight fractions of Fe₂SiO₄ and FeO phases decreased while Al-rich protective oxide phases (Al₂SiO₅, Al₂FeO₄ and AlFeO₃) increased. Thermogravimetric analyses determining the oxidation kinetics showed that SiNb alloy had lower oxidation tendency compared to SiMo alloy, and this tendency is drastically decreased by the addition of aluminum in SiNb alloy.
3. Two layered and porous oxide scales formed on the surfaces were observed, and the presence of Fe₂O₃, Fe₃O₄, FeO and Fe₂SiO₄ oxide phases as similar to thermodynamic calculations were detected. In SiNb-*x*Al alloys, oxide scale got thinner compared to SiMo and SiNb, and due to the change in graphite morphology from nodular to vermicular, oxidation progressed toward matrix through vermicular graphite. The Al-rich oxide forms (Al₂SiO₅, Al₂FeO₄ and AlFeO₃) were present in the SEM/EDS data supporting the thermodynamic calculations.

The results revealed that all designed alloys exhibited better oxidation resistance at all investigated temperatures than commercial SiMo alloy, and as aluminum addition increases, better performance is obtained because of the formation of Al-rich protective oxide layers. Thus, the designed alloys can be suggested as alternative exhaust manifold materials at elevated temperatures.

ACKNOWLEDGMENTS

The authors, G. Aktaş Çelik, Ş. Polat and Ş. H. Atapek, wish to acknowledge the financial support given by Scientific Research Projects Coordination Unit of Kocaeli University under the Project Nos. 2017/118 and 2019/118.

CONFLICT OF INTEREST

On behalf of all authors, the corresponding author states that there is no conflict of interest.

REFERENCES

1. A.A. Partoaa, M. Abdolzadeh, and M. Rezaeizadeh: *J. Cent. South. Univ.*, 2017, vol. 24, pp. 546–59.
2. Y. Zhang, M. Li, L.A. Godlewski, J.W. Zindel, and Q. Feng: *Metall. Mater. Trans. A.*, 2016, vol. 47A, pp. 3289–94.
3. M. Ekström and S. Jonsson: *Mater. Sci. Eng. A.*, 2014, vol. 616, pp. 78–87.
4. I. Patil and D.S. Bhat: *IRJET.*, 2020, vol. 7, pp. 4960–64.
5. I. Anieken, O.E. Kelly, and G. Abdulsamad: *Int. J. Eng. Technol.*, 2017, vol. 3, pp. 50–60.
6. G. Burton Bortham, P.O. Ransone, and H.K. Rivers: *USA Patent*, 1999, p. 5927070.
7. L.M. Åberg and C. Hartung: *Trans. Indian Inst. Met.*, 2012, vol. 65, pp. 633–36.
8. J.P. Shingledecker, P.J. Maziasz, N.D. Evans, and M.J. Pollard: *Int. J. Press. Vessels Pip.*, 2007, vol. 84, pp. 21–28.
9. M.M. Ibrahim, A. Nofal, and M.M. Mourad: *Metall. Mater. Trans. B.*, 2017, vol. 48B, pp. 1149–57.
10. M. Ekström, P. Szakalos, and S. Jonsson: *Oxid. Met.*, 2013, vol. 80, pp. 455–66.
11. F. Tholence and M. Norell: *Oxid. Met.*, 2008, vol. 69, pp. 13–36.
12. Y. Zhang, M. Li, L.A. Godlewski, J.W. Zindel, and Q. Feng: *Mater. Sci. Eng. A.*, 2017, vol. 683, pp. 195–206.
13. F. Tholence and M. Norell: *Oxid. Met.*, 2008, vol. 69, pp. 37–62.
14. Y.L. Yang, Z.Y. Cao, Z.S. Lian, and H.X. Yu: *Adv. Mater. Res.*, 2011, vol. 194–196, pp. 95–99.
15. G.A. Çelik, M.I.T. Tzini, Ş. Polat, J.S. Aristeidakis, ŞH. Atapek, P.I. Sarafolou, and G.N. Haidemenopoulos: *J. Min. Metall. Sect. B.*, 2021, vol. 57, pp. 53–62.
16. V. Gautam, S. Ahuja, and N. Ram: *ELK Asia Pac. J.*, 2017, vol. 978–93, pp. 85537-06–85546.
17. T. Seifert and H. Riedel: *Int. J. Fatigue.*, 2010, vol. 32, pp. 1358–67.
18. G.M. Castro Güiza, W. Hormaza, A.R. Galvis, and L.M. Méndez Morenod: *Eng. Fail. Anal.*, 2017, vol. 822, pp. 138–48.
19. M. Stawarz: *Arch. Foundry Eng.*, 2017, vol. 17, pp. 147–52.
20. R. González-Martínez, U. Torre, J. Lacaze, and J. Sertucha: *Mater. Sci. Eng. A.*, 2018, vol. 712, pp. 794–802.
21. R. González-Martínez, U. Torre, J. Lacaze, and J. Sertucha: *Mater. Sci. Eng. A.*, 2018, vol. 712, pp. 803–11.
22. P. Matteis, G. Scavino, A. Castello, and D. Firrao: *Metall. Mater. Trans. A.*, 2015, vol. 46A, pp. 4086–94.
23. M. Ekström: Development of a Ferritic Ductile Cast Iron for Increased Life in Exhaust Applications, Licentiate Thesis, Royal Institute of Technology, Stockholm, Sweden, 2013, ISBN 978-91-7501-711-2.
24. G. Aktaş Çelik, M.-I. T.Tzini, Ş.H. Atapek, Ş. Polat, and G.N. Haidemenopoulos: in *Proc. IMMC19*, 2018, pp.1086-89.
25. G. Aktaş Çelik, M.-I.T. Tzini, ŞH. Atapek, Ş. Polat, and G.N. Haidemenopoulos: *Int. J. Miner. Metall. Mater.*, 2020, vol. 27, pp. 190–99.
26. G. Aktaş Çelik, M.-I.T. Tzini, ŞH. Atapek, Ş. Polat, and G.N. Haidemenopoulos: *Metall. Mater. Eng.*, 2020, vol. 26, pp. 15–29.
27. S.N. Lekakh, A. Bofah, W.-T. Chen, L. Godlewski, and M. Li: *Int. Metalcast.*, 2021, vol. 15, pp. 874–88.
28. C. Delprete and R. Sesana: *Mater. Des.*, 2014, vol. 57, pp. 528–37.
29. A.R. Kiani Rashid and D.V. Edmonds: *Surf. Interface Anal.*, 2004, vol. 36, pp. 1011–13.
30. M.S. Soiński, A. Jakubus, and G. Stradomski: *Arch. Foundry Eng.*, 2013, vol. 32, pp. 163–68.
31. G. Aktaş Çelik: Egzoz manifoldu olarak kullanılan sünek dökme demirlerin alaşımlama ile geliştirilmesi, PhD Thesis, 2020, Kocaeli, Turkey.
32. N. Haghdadi, B. Bazaz, H.R. Erfanian-Naziftoosi, and A.R. Kiani-Rashid: *Int. J. Miner. Metall. Mater.*, 2012, vol. 19, pp. 812–20.
33. A.R. Kiani-Rashid: *J. Alloy Compd.*, 2009, vol. 470, pp. 323–27.
34. A. Shayesteh-Zeraati, H. Naser-Zoshki, A.R. Kiani-Rashid, and M.R. Yousef-Sani: *J. Mater.: Des. Appl.*, 2010, vol. 224, pp. 117–22.
35. A. Shayesteh-Zeraati, H.N. Zoshki, and A.R. Kiani-Rashid: *J. Alloys Compd.*, 2010, vol. 500, pp. 129–33.
36. H. Nakae and H. Shin: *Mater. Trans.*, 2001, vol. 42, pp. 1428–34.
37. D. Holmgren, A. Diószegi, and I.L. Svensson: *Int. J. Cast Met. Res.*, 2007, vol. 20, pp. 30–40.
38. C.G. Schön and A. Sinatora: *Calphad.*, 1998, vol. 22, pp. 437–48.
39. A. Bedolla-Jacuinde, M.W. Rainforth, and I. Mejia: *Metall. Mater. Trans. A.*, 2013, vol. 44A, pp. 856–72.
40. J. Feng, C. Pan, L. Lu, Q. Huang, and H. Cao: *J. Iron. Steel Res. Int.*, 2016, vol. 23, pp. 618–24.
41. M.M. Ibrahim, M.M. Mourad, A.A. Nofal, and A.I.Z. Farahat: *Int. J. Cast Met. Res.*, 2017, vol. 30, pp. 61–69.
42. L.L. Liu and Q.Q.Y. Guo Niu: *Oxid. Met.*, 2013, vol. 79, pp. 201–24.
43. S. Mendez, M.A. Arenas, A. Niklas, R. González, A. Conde, J. Sertucha, and J.J.D. Damborenea: *Oxid. Met.*, 2019, vol. 91, pp. 225–42.
44. A. Ebel, S.Y. Brou, B. Malard, J. Lacaze, D. Monceau, and L. Vaissière: *Mater. Sci. Forum.*, 2018, vol. 925, pp. 353–60.
45. O. Tsurtsumia, F. Pedraza, B. Gregoire, N. Khidasheli, and E. Kutelia: *Metall. Mater. Trans. A.*, 2020, vol. 51A, pp. 920–26.
46. M.-B. Lin, C.-J. Wang, and A.A. Volinsky: *Oxid. Met.*, 2011, vol. 76, pp. 161–68.
47. R. Prescott and M.J. Graham: *Oxid. Met.*, 1992, vol. 38, pp. 73–87.
48. P. Tomaszewicz and G.R. Wallwork: *Oxid. Met.*, 1983, vol. 19, pp. 165–85.

Publisher's Note Springer Nature remains neutral with regard to jurisdictional claims in published maps and institutional affiliations.